

1 Whistler scattering of suprathermal electrons in the
2 solar wind: particle-in-cell simulations

Shinji Saito and S. Peter Gary

3 Los Alamos National Laboratory, Los Alamos, NM 87545, USA

Shinji Saito, Los Alamos National Laboratory, Los Alamos, NM 87545, USA. (ssaito@lanl.gov)

S. Peter Gary, Los Alamos National Laboratory, Los Alamos, NM 87545, USA.
(pgary@lanl.gov)

Abstract. Solar wind observations sometimes show that suprathermal, magnetic-field-aligned, strahl electrons have pitch-angle distributions which become broader in width as electron kinetic energy increases. Magnetosonic-whistler waves propagating sunward at $\mathbf{k} \times \mathbf{B}_0 = 0$ where \mathbf{B}_0 is the background magnetic field and \mathbf{k} is the wavenumber have a cyclotron resonance with electrons propagating in the anti-sunward direction. This resonance leads to pitch-angle scattering which increases strahl electron energy perpendicular to \mathbf{B}_0 . The strahl response to a broadband whistler fluctuation spectrum was studied using Particle-In-Cell (PIC) simulations in a magnetized, homogeneous, collisionless plasma. The simulations show that enhanced whistler waves with finite damping lead to strahl distributions which broaden in width with increasing kinetic energy, in agreement with certain observations. Results from the simulations show how the strahl is broadened as a function of wave amplitude and relative strahl density.

1. Introduction

Electron velocity distributions below 1keV in the solar wind are often observed to consist of a cool dense core component ($T \sim 10\text{eV}$) and hotter, more tenuous suprathermals. The core electrons have a nearly Maxwell velocity distribution due to particle-particle collisions. Above the core/suprathermal breakpoint (typically between 60 to 80 eV), particle-particle collisions are not so effective [Ogilvie *et al.*, 2000] and the suprathermals are often observed to be non-Maxwellian, consisting of two distinguishable components, a halo and a strahl [Feldman *et al.*, 1978]. The halo component is almost isotropic, whereas the strahl component is anisotropic with a narrow pitch-angle distribution directed away from the Sun along the background magnetic field \mathbf{B}_0 .

The narrowness of the strahl is due to conservation of the first adiabatic invariant which decreases the perpendicular speed of the electrons as they propagate away from the Sun into regions of decreasing magnetic field. However, strahl widths are broader than the widths which are predicted by this conservation. Collisional effects are not sufficient to describe the broadened strahl distributions in the solar wind [Lemons and Feldman, 1983], suggesting that wave-particle interactions are important to scatter such electrons.

The widths of strahl pitch-angle distributions vary with solar wind conditions. Pilipp *et al.* [1987a, 1987b], using data from Helios 2, found a clear correlation between the strahl width and magnetic structures in the solar wind. The strahl almost disappears at sector boundaries of the interplanetary magnetic field, whereas in the interior of the sectors far from boundaries, suprathermal electrons are extremely anisotropic and form a narrow

strahl. They also suggest that particle-particle collisions are not sufficient to account for the observations.

Crooker et al. [2003] studied suprathermals in more detail using Wind spacecraft data. They showed that suprathermal electron anisotropy changes not only at magnetic field sector boundaries, but also with small scale variations of plasma β in the solar wind. They also demonstrated that high β plasmas are correlated with more isotropic suprathermal electrons, but they did not address possible sources of this correlation.

An observable property which provides insight into the processes responsible for strahl broadening is the width of the pitch-angle distribution as a function of electron kinetic energy. As demonstrated by *Ogilvie et al.* [2000], the scattering effectiveness of particle-particle collisions decreases rapidly with electron energy above the core/suprathermal breakpoint energy. Thus, collisional scattering alone should lead to strahl pitch-angle distributions which become narrower as electron energy increases. *Ogilvie et al.* [2000] showed that the energy extent of this effect is a function of the average solar wind density, but for average solar wind parameters, it is likely that the observations of such strahl extending up to a few hundred eV [e.g., *Feldman et al.*, 1978; *Lemons and Feldman*, 1983; *Pilipp et al.*, 1987a, b] are indicative of collisional scattering.

In contrast, both quasilinear models [*Vocks et al.*, 2005] and particle-in-cell simulations [*Saito and Gary*, 2006] demonstrate that a broadband spectrum of whistler fluctuations scatter suprathermal electrons with an efficacy that increases as electron kinetic energy increases, leading to strahl pitch-angle distributions which increase in width with increasing electron energy. More recent observations which extend to higher energies of the order of a kilovolt show that strahl with such characteristic broadening can be measured in the

solar wind [*Olgivie et al.*, 2000; *Vocks et al.*, 2005; *Pagel et al.*, 2005, 2007]. And at still higher energies above 1 keV, *Lin* [1998] reported observations of an isotropic superhalo, apparently corresponding to complete pitch-angle scattering of the strahl.

One of the most likely scattering processes for suprathermal electrons is wave-particle interactions with magnetosonic-whistler waves. Electron cyclotron wave-particle interactions are the most effective when the electron velocity parallel to \mathbf{B}_0 , $v_{||,e}$, satisfies the cyclotron resonance condition,

$$k_{||}v_{||,e} = \omega_r + \Omega_e, \quad (1)$$

where $k_{||}$, ω_r , and Ω_e are the wave number parallel to the background magnetic field, the real frequency which is a function of $k_{||}$, and the electron cyclotron frequency, respectively. A quasilinear theory which describes the interaction between solar wind electrons and whistler fluctuations coming from the solar corona with the condition $\mathbf{k} \times \mathbf{B}_0 = 0$ [*Vocks and Mann*, 2003] indicates the formation of a strahl distribution with extremely narrow pitch-angle width. The electrons scattered by the whistler waves are focused by the mirror force of the decreasing magnetic field in interplanetary space. *Vocks et al.* [2005] further introduce sunward propagating whistler waves into their quasilinear theory; these fluctuations scatter the strahl, leading to a more isotropic distribution at higher energies.

There are, at least, two potential sources of enhanced whistler fluctuations in the solar wind: wave-particle interactions and wave-wave interactions. The first can generate magnetic fluctuations through electromagnetic instabilities, such as the whistler heat flux instability and the whistler anisotropy instability. The whistler heat flux instability is driven by a halo/core relative drift [*Gary et al.*, 1975a,b]. *Gary et al.* [1999] hypothesizes that the instability threshold derived from linear theory corresponds to an upper

bound on the heat flux in the solar wind. However, by comparing the electron heat flux with wave activity, *Scime et al.* [2001] used Ulysses data to conclude that the whistler heat flux instability does not contribute to constraining the solar wind heat flux. The whistler anisotropy instability driven by the core anisotropy $T_{\perp}/T_{\parallel} > 1$ may also enhance whistler waves; such anisotropic distributions may be driven by interplanetary shocks in the solar wind. *Saito and Gary* [2006] used a Particle-In-Cell simulation to show that whistler waves enhanced by the anisotropic distribution of core electrons can broaden the low energy strahl. But the enhanced fluctuations are at wavenumbers too large to scatter strahl electrons with relatively higher energies. Therefore, it appears that electromagnetic instabilities do not strongly scatter the suprathermal electrons at relatively high energies.

Another potential source of enhanced whistler waves are magnetic fluctuations cascading through wave-wave interactions. At relatively low frequencies, the magnetic power spectrum in the solar wind is often observed to have a power law dependence $f^{-5/3}$ (e.g. *Smith et al.*, 2006a,b), which is referred to as the "inertial range" of solar wind turbulence. At higher wave frequencies, the power spectrum become steeper than in the inertial range. If the wave energy reaches whistler frequencies through wave-wave interactions, such fluctuations can scatter higher energy strahl electrons, as suggested by observations [*Pagel et al.*, 2007], quasilinear theory [*Vocks et al.*, 2005], and a self-consistent simulation [*Saito and Gary*, 2006].

The quasilinear theory of *Vocks and Mann* [2003] and *Vocks et al.* [2005] uses non-damped whistler waves to scatter strahl electrons. But there are two reasons why damping of the waves is an important part of the scattering process. One is that damping limits the energy of the resonant waves available for scattering, and the other is that damping

introduces a broad width in the resonance velocity. The scattering should depend on the amount of wave energy converted into electron kinetic energy, and the broad resonance velocity function for damped waves should lead to a more realistic velocity distribution rather than the sharp resonance velocity function associated with undamped fluctuations.

In order to understand the pitch-angle scattering process, fully self-consistent calculations are needed. We have done self-consistent particle-in-cell simulations to examine the cyclotron resonance between whistler waves with a power law wavenumber dependence and suprathermal electrons with narrow pitch-angle distributions. In particular, this manuscript describes how such whistler fluctuation spectra broaden strahl pitch-angle distributions as a function of both wave amplitude and strahl density.

2. Simulation model

To study the interaction between broadband whistler fluctuations and suprathermal electrons, we use a three-dimensional, collisionless, relativistic particle-in-cell code. Periodic boundary conditions are imposed for all directions. We assume a collisionless, electron-proton plasma. The electrons consist of three components, a cool and dense Maxwellian core distribution denoted by subscript c , a tenuous and hot Maxwellian component (subscript h), and a tenuous and anisotropic bi-Maxwellian strahl component (subscript s) which has a drift velocity directed away from the Sun. Subscript e represents overall electron properties, for instance, $n_e = n_c + n_h + n_s$. The proton density n_p is equal to n_e .

The mass ratio m_p/m_e is equal to 1836. We choose $\beta_p = 0.5$, an appropriate average value for the solar wind. The ratio of the electron plasma and cyclotron frequencies is $\omega_e/|\Omega_e| = 10.0$. The proton temperature T_p is equal to the electron core temperature T_c ,

and the both distributions are isotropic. The halo component is also isotropic but the temperature is 10 times higher than core electrons, $T_h/T_c = 10$. The parallel temperature of the strahl is $T_{\parallel,s}/T_c = 3$, and the strahl is anisotropic $T_{\parallel,s}/T_{\perp,s} = 10$, where subscripts \parallel and \perp denote components parallel and perpendicular to the background magnetic field \mathbf{B}_0 . The strahl component has an average drift velocity in the antisunward negative direction, $v_{0,s}/v_c = -2$. To satisfy the zero electric current condition at $t = 0$, the mean velocity of core electrons is taken as $v_{0,c} = -(n_s v_{0,s})/n_c$. The electron component densities are variables for the several simulations in this paper.

The computation time step is $\delta t = 0.05/\omega_e$. A grid size Δ corresponds to $0.1\omega_e/c$ (c is the light velocity). The electron Debye length v_e/ω_e is equal to 0.5Δ . The background magnetic field is along the x direction $\mathbf{B}_0 = (B_o, 0, 0)$. The numbers of grids for each direction are $L_x = 4096$, $L_y = 3$, and $L_z = 3$.

Whistler fluctuations are imposed into the simulation at $t=0$. The electric and magnetic fluctuation for the waves are

$$\delta \mathbf{B}(x) = \sum_n \delta B_n [\hat{\mathbf{y}} \sin(k_n x + \phi_n) + \hat{\mathbf{z}} \cos(k_n x + \phi_n)] \quad (2)$$

$$\delta \mathbf{E}(x) = \sum_n \delta E_n [\hat{\mathbf{y}} \cos(k_n x + \phi_n) - \hat{\mathbf{z}} \sin(k_n x + \phi_n)] \quad (3)$$

where δB_n is the amplitude of a magnetic fluctuation, and k_n is the wavenumber of a whistler wave propagating parallel to x direction. Here $\delta E_n = (|\omega|/k_n c) \delta B_n$ and $|\omega| = \sqrt{\omega_r^2 + \gamma^2}$. The initial velocity perturbation for each species in response to each mode is

$$|\delta v_{j,n}| = \left| -\frac{i\Omega_j \delta B_n}{k_n B_o} \left[\left(\frac{\omega - k_n v_{d,j}}{\sqrt{2} k_n v_j} + \left(\frac{T_{\perp,j}}{T_{\parallel,j}} - 1 \right) \zeta_{j,n}^+ \right) Z(\zeta_{j,n}^+) + \left(\frac{T_{\perp,j}}{T_{\parallel,j}} - 1 \right) \right] \right|. \quad (4)$$

where ω , $\zeta_{j,n}^+$, and $Z(\zeta_{j,n}^+)$ are obtained from linear dispersion theory.

Figure 1 illustrates a velocity-space model of the interaction. We define the sunward and the antisunward directions as positive and negative, respectively. At $t = 0$ we impose whistler fluctuations propagating at $\mathbf{k} \times \mathbf{B}_0 = 0$ in the sunward direction. The contour lines represent the electron velocity distribution, with the strahl component encircled by the dashed line. Phase speeds of whistler waves with representative wavenumbers k_0 and k_1 are indicated by straight dashed lines, and the two straight solid lines indicate the corresponding cyclotron resonance velocities of the electrons. In order to satisfy the resonance condition [equation (1)], the resonance velocity must be negative (antisunward) when the whistler waves propagate in the positive (sunward) direction. Fluctuations with smaller wavenumbers scatter electrons with higher velocities parallel to the background magnetic field. In order to obtain the dispersion relations for the whistler waves, we use linear Vlasov dispersion theory as discussed in section 3.

3. Linear theory and whistler fluctuations

The linear dispersion equation for electromagnetic fluctuations propagating in a collisionless, homogeneous plasma is, at $\mathbf{k} \times \mathbf{B}_0 = 0$,

$$\omega^2 - k^2 c^2 + k^2 c^2 \sum_j S_j^\pm(\mathbf{k}, \omega) = 0 \quad (5)$$

where the sum is over each charged particle species or component j . We assume that the velocity distribution of each component is a bi-Maxwellian,

$$f_j(v_\parallel, v_\perp) = \frac{n_j}{(2\pi v_j^2)^{3/2}} \frac{T_{\parallel,j}}{T_{\perp,j}} \exp \left[-\frac{v_\parallel^2}{2v_j^2} - \frac{v_\perp^2}{2v_j^2} \frac{T_{\parallel,j}}{T_{\perp,j}} \right]. \quad (6)$$

where v_j is a thermal velocity of each component j . The dimensionless conductivity [Gary, 1993] is

$$S_j^\pm(k_{||}, \omega) = \frac{\omega_j^2}{k_{||}^2 c^2} \left[\zeta_j Z(\zeta_j^\pm) + \left(1 - \frac{T_{||,j}}{T_{\perp,j}} \right) \frac{Z'(\zeta_j^\pm)}{2} \right] \quad (7)$$

where $Z(\zeta)$ is the plasma dispersion function, $\zeta_j^\pm = (\omega - k_{||}v_{0,j} \pm \Omega_j)/(\sqrt{2}|k_{||}|v_j)$, $v_{0,j}$ is the average velocity parallel to the magnetic field for component j , and \pm indicates the polarization of the fluctuations. Here we use " + " to denote right-handed polarization.

Figure 2 shows whistler dispersion properties and ζ_j^+ derived from Equation (5) with the parameters: $(n_c, n_h, n_s)/n_e = (0.9, 0.1, 0.0)$ (left column) and $(n_c, n_h, n_s)/n_e = (0.85, 0.1, 0.05)$ (right column). At long wavelengths, $ck/\omega_e < 0.1$, there are few suprathermal electrons to resonate with the waves, so the damping is very weak in both cases. In the case without the strahl component, $n_s = 0.0$, the damping starts to increase at $ck/\omega_e > 0.5$, corresponding to $|\zeta_c^+| \leq 3$, indicating the beginning of a cyclotron resonance by the core component. Although $|\zeta_h^+|$ is always smaller than $|\zeta_c^+|$, the halo component does not cause much damping of the whistler waves. The reason is that the halo is so tenuous and hot that only a few particles can resonate with the waves. In the case with a strahl component, there appears a clear difference in the damping rate, even though both ζ_c^+ and ζ_h^+ are almost the same as the other case. The damping begins at $ck/\omega_e > 0.2$ where $|\zeta_s^+|$ starts to be less than 3. This clearly indicates that the strahl component causes the damping onset for the whistler waves shown in the upper right-hand panel of Figure 2.

4. Simulation results

In this section, we show simulation results for strahl scattering with imposed whistler fluctuations. First, we show the scattering of a strahl component by a monochromatic whistler wave, illustrating the basic interaction. Second, we impose an enhanced broadband spectrum of thirty whistler modes on the system. In the solar wind, magnetic power spectra are continuous functions of frequency, so we use such a multimode spectrum to make contact with observations. We study the dependence of strahl scattering on the fluctuation energy and the relative strahl density n_s/n_e .

4.1. Strahl electrons scattering by a monochromatic whistler wave

The first three simulations, Runs A, B, and C, address pitch-angle scattering by a monochromatic whistler wave of successively shorter wavelength, as described in Table 1. The electron component densities are $n_c/n_e = 0.85$, $n_h/n_e = 0.1$, and $n_s/n_e = 0.05$ in all three simulations. The other plasma parameters are as listed above. To calculate the responses of all components with accuracy, we need to use many superparticles for the tenuous halo and strahl components. We load the superparticles for electrons in the simulations with the number densities N which are $N_c = 85$, $N_h = 100$, and $N_s = 100$.

Figure 3 shows the electron velocity distributions at $t|\Omega_e| = 0.0$ (left) and 100.0 (right) for the three cases, Run A (top), B (middle), C (bottom) respectively. At $t|\Omega_e| = 0.0$, the strahl distribution for Run C is somewhat broader than the distribution for Run A, due to the initial velocity perturbation [Equation(4)]. The figures show clear differences in the strahl scattering among three cases, due to the differences in the resonance velocities for the imposed whistler wave. From Equation (1) the resonance velocities for Runs A, B, and C are $v_{res}/v_c = 12.774$, 6.140, and 3.680, respectively. Even though the resonance velocity

is far from the strahl distribution in the case of Run A, the distribution becomes somewhat broader at $t|\Omega_e| = 100.0$. In the case of Run B and C, the electrons are scattered not only at each resonance velocity but also on a broad range of velocity space.

This broad range of scattering may be interpreted through the use of the electron scattering factor derived in the Appendix. This factor is important in determining the strength of the wave-particle interaction and the width of the scattering in resonant velocity. Figure 4 shows scattering factors of each wave in the three Runs. The dashed, solid, and bold lines show this factor for Runs A, B, and C, respectively. The velocities where peak values are located correspond to the resonance velocities derived from equation (1). This figure shows that the scattering factor of the wave for Run A has a sharp distribution, and the wave resonates only with relatively high energy electrons. Therefore, the strahl distribution in Run A shown in Figure 3 is only weakly scattered. In the other two cases, as $|\zeta_s^+|$ decreases, the damping rate increases, the width of the scattering factor becomes broader and the strahl electrons are scattered by the whistler wave in a broader range of velocity space. If the damping were neglected, the scattering factor would form a very sharp distribution, like a delta function, and the whistler wave would only scatter electrons with precisely the resonant velocity. These results indicate that inclusion of self-consistent damping is very important for study of strahl scattering.

4.2. Strahl electrons scattering by a whistler wave spectrum

We next present results from simulations in which we use multiple modes to impose a broadband power spectrum at $t = 0$. The initial power spectrum is of the form

$$\frac{|\delta B|^2}{B_o^2} = S_B \sum_{n=1}^{nmax} \left(\frac{k_n c}{\omega_e} \right)^{-\alpha}. \quad (8)$$

We choose $\alpha = 3$, $nmax = 30$, $k_1c/\omega_e = 0.15339$, and $k_{30}c/\omega_e = 0.59824$ in all simulations shown below. k_n is defined as $k_n = k_1 + (n - 1)\Delta k$, where $\Delta kc/\omega_e = 0.0153396$. S_B is a variable which determines the total magnetic fluctuation energy. The other parameters such as system size, plasma β , etc. are same as those introduced in section 2.

Although these modes are discrete, almost all fluctuations have a nonzero damping rate. It means that the electron scattering factor of each mode has a finite width in $v_{||}$, as shown in the above section. This implies that electron scattering by this discrete fluctuation spectrum should emulate the consequences of scattering by the essentially continuous power spectrum of magnetic fluctuations in the solar wind.

4.2.1. Strahl broadening as function of wave amplitude

This subsection describes results from four simulations in which the only initial parameter which is varied is the total energy of the initial magnetic fluctuations. We use an electron distribution with $(n_c, n_h, n_s)/n_e = (0.85, 0.10, 0.05)$. The individual fluctuations of the imposed whistler spectrum follow the dispersion relation and ζ_j^+ shown in the right-hand side of Figure 2. Figure 5 shows contour plots of electron velocity distributions at $t|\Omega_e| = 0$ and 100.0 in two cases, $|\delta B|^2/B_0^2 = 0.005$ and 0.01. In both cases, the strahl component is clearly broader at $t|\Omega_e| = 100.0$, and the stronger wave energy leads to greater pitch-angle scattering.

Strong damping of the short wavelength whistlers depletes the energy in this part of the spectrum. Figure 6 shows the wave spectra at $t = 0$ (solid lines) and $t|\Omega_e| = 100$ for all four cases. Open triangles, solid triangles, open circles, and solid circles show the spectra with initial wave energies, $|\delta B|^2/B_0^2 = 0.0025, 0.005, 0.01$, and 0.02 respectively. The

227 wave energy at $ck/\omega_e \geq 0.3$ has been damped at late-times in all four cases, as predicted
 228 by linear theory shown in the upper right-hand panel of Figure 2.

229 Note that the late-time power spectra in the short wavelength damped regime decrease
 230 faster than any power law in wavenumber. This result is very similar to that obtained by
 231 *Li et al.* [2001] using an analytic model for dissipation of turbulence. Figure 6 supports
 232 the conclusion of *Li et al.* [2001] that short wavelength power law fluctuation spectra
 233 observed in the solar wind are not necessarily indicators of turbulent dissipation.

234 Figure 7 shows electron pitch-angle widths as a function of kinetic energy, at $t|\Omega_e| = 0$
 235 (open circles) and 100.0 (solid circles) in two cases, as labeled. The whistler spectrum with
 236 the larger wave amplitude clearly leads to a broader strahl distribution at all energies.
 237 Further, in both cases the strahl width becomes larger as the kinetic energy increases, as
 238 demonstrated in *Saito and Gary* (2006).

239 Figure 8 shows the pitch-angle width with three energies, $(v_{\parallel}^2 + v_y^2)/v_c^2 = 20$ (open
 240 triangles), 30 (open circles), and 40 (solid circles), as a function of initial wave energy.
 241 The width at higher kinetic energies is broader than at lower energies; however, the
 242 increase in width is not linear with the initial wave energy. To understand this effect, we
 243 introduce the electron scattering factor σ_e , derived in the Appendix.

244 Figure 9 shows electron scattering factors for three modes as functions of the parallel
 245 velocity. This factor, which is important in determining the strength of the wave-particle
 246 interaction, becomes broader and smaller as k increases and $|v_{\parallel}|$ decreases. Pitch-angle
 247 scattering causes a decrease in the velocity, so that the electrons scattered into higher
 248 pitch-angles interact with waves which have smaller scattering factors and wave ampli-
 249 tudes. In addition the damping rates also increase with decreasing parallel velocity as

shown in Figure 9. This means that the short wavelength modes have even smaller amplitudes and the scattering gets weaker as time increases. As a result, shorter wavelength modes disappear before the electrons scattered from lower pitch-angles strongly interact with those modes. Therefore, the scattering becomes weaker as the pitch-angle increases and is not directly proportional to the initial fluctuation energy.

4.2.2. Strahl broadening as function of strahl density

This subsection describes results from three simulations in which the strahl density is varied as $n_s/n_e = 0.03, 0.05, \text{ and } 0.07$. The dispersion relation varies with the strahl density, so we derive the frequencies and damping rates for each run, and use it for the initially imposed whistler fluctuations. For the three runs the total electron density n_e and halo density n_h are kept constant, but the core component n_c is varied in order to maintain a constant n_e . We use a fixed initial wave energy $|\delta B|^2/B_o^2 = 0.01$.

Figure 10 shows electron velocity distributions at $t|\Omega_e| = 0.0$ (left column) and 100.0 (right column) from runs with $n_s/n_e = 0.03$ (top) and $n_s/n_e = 0.07$ (bottom). The strahl are clearly broadened in both cases, and at the higher energies most of the strahl electrons are scattered and disappear into the halo. But at lower energies, in the higher density case the strahl remains more clearly as a discernable, anisotropic component.

Figure 11 displays strahl pitch-angle widths from the simulations with $n_s/n_e = 0.03$ (left) and 0.07 (right) as functions of kinetic energy. As in Figure 7, the strahl distribution after scattering (shown as solid circles) becomes broader with increasing kinetic energy. Further, over all energies, the late-time pitch angle widths with $n_s/n_e = 0.03$ are larger than those with $n_s/n_e = 0.07$. This relation is further illustrated in Figure 12 which shows the relationship between strahl density and pitch angle width after scattering at

three energies: open triangles, open circles, and solid circles represent the pitch-angle width with energies $(v_{\parallel}^2 + v_y^2)/v_c^2 = 20, 30, \text{ and } 40$ respectively. At each energy, the pitch-angle width increases with decreasing strahl density. This result is associated with the scattering factor as shown in Figure 13. Open triangles, open circles, and solid circles indicate the maximum value of the factor for each mode with $n_s/n_e = 0.03, 0.05, \text{ and } 0.07$. More tenuous strahl correspond to weaker damping rates, and therefore larger scattering factors at resonance. Thus the strahls should be more strongly scattered at smaller relative densities.

5. Conclusions

We have studied suprathermal electron responses to both a single whistler mode and a broadband whistler spectrum by using particle-in-cell simulations in a homogeneous, collisionless plasma. We have imposed whistler fluctuations at $t = 0$ and self-consistently computed the plasma response to demonstrate wave-particle scattering of strahl electrons in the solar wind. In such a computation, the damping rate of each fluctuation is important in the interpretation of the scattering. The electron scattering factor becomes broader in velocity as the damping rate increases; as a consequence of this broadening, the electrons are scattered away from the resonance condition defined by equation (1).

We have demonstrated broadening of strahl distributions by interaction with both a single whistler wave and a broadband whistler fluctuation spectrum with k^{-3} dependence. The cyclotron resonance condition implies that electrons with larger $|v_{\parallel}|$ resonate with fluctuations of smaller k_{\parallel} ; because the longer wavelength modes have larger wave amplitudes, there is stronger scattering at higher energies. Thus, strahl broadening with increasing kinetic energy is a natural consequence of scattering by such a spectrum. We

note that several observations of strahl pitch-angle distributions at 1AU which do not show such broadening [*Feldman et al.*, 1978; *Lemons and Feldman*, 1983; *Hammond et al.*, 1996] are limited to electron energies below 250eV. In contrast, some observations up to kinetic energies of the order of 1 keV [*Olgivie et al.*, 2000; *Vocks et al.*, 2005; *Pagel et al.*, 2005, 2007] show strahl widths which increase with energy. Further, *de Koning et al.* [2006, 2007] find that pitch-angle distributions become broader at higher kinetic energies during some suprathermal electron bursts. Magnetic power spectra in the solar wind have the almost universal property that they decrease in magnitude as the frequency or wavenumber increase. Therefore, we hypothesize that, for sufficiently large kinetic energies, an increasing strahl width with increasing energy is a universal property of electron distributions in the solar wind.

As the initial magnetic fluctuation energy in our simulations becomes larger, the strahl pitch angle width becomes larger over all energies, but this broadening does not increase in proportion to the wave energy. Both the wave spectrum and the damping rate contribute to this trend. When the electrons are scattered, their parallel velocities decrease with increasing pitch-angles. Then, these electrons successively interact with whistler fluctuations with larger wavenumbers which have smaller scattering factors. Thereby the scattering becomes weaker as the pitch-angle becomes larger. In addition, fluctuations with larger wavenumbers have larger damping rates, so that the wave amplitude decreases in time. Therefore, the damping effect also leads to the weakness of the scattering at high pitch-angle.

The broadening process becomes more effective as the strahl density decreases. This can be interpreted in terms of the electron scattering factor which develops a larger peak

with decreasing strahl density due to the reduction in the damping rate. Thus the strahl electrons are scattered more strongly as the strahl density decreases.

If fluctuation damping were neglected, as is done in some models, undamped waves would continue to scatter the strahl electrons to smaller v_{\parallel} and resonances at larger k_{\parallel} . In this case, the maximum wavenumber of a power spectrum would determine the pitch-angle widths at all energies. For instance, if the resonant velocity were nearly zero and the model allowed enough time for scattering, strahl pitch-angles would almost reach 90 degrees independent of wave amplitude or strahl density. But this contradicts the results of our simulations. So quasilinear theories that neglect damping provide a less complete description of the scattering process, then do self-consistent calculations such as particle-in-cell simulations.

Further simulations should address the important questions of how whistler scattering might lead to the formation of the relatively isotropic halo component and whether such scattering may contribute to electron acceleration. In particular, particle-in-cell simulations could be used to study whether electron scattering by whistler fluctuations might be the source of the anticorrelation between the anisotropy of the strahl component and the plasma β observed by *Crooker et al* [2003].

6. Appendix: Electron scattering factor

Equation (1) describes the v_{\parallel} of electrons which are in cyclotron resonance with a fluctuations of a particular frequency and wavenumber. To obtain a rough estimate of the strength of the resulting wave-particle interaction, we here derive what we call the electron scattering factor.

We consider an electric fluctuation \mathbf{E} propagating parallel to the background magnetic field $\mathbf{B}_0 = (B_0, 0, 0)$ and an electron velocity \mathbf{v} with helical motion,

$$\mathbf{E} = (0, \delta E e^{\gamma t} \cos(kx - \omega_r t), -\delta E e^{\gamma t} \sin(kx - \omega_r t)) \quad (9)$$

$$\mathbf{v} = (v_{||}, -v_{\perp} \cos(\Omega_e t + \phi), v_{\perp} \sin(\Omega_e t + \phi)) \quad (10)$$

where δE and γ (< 0) are an initial amplitude and a damping rate of the fluctuation. ω_r and k are a real part of frequency and wavenumber parallel to the background magnetic field. $v_{||}$ and ϕ are constants, and we define the electron cyclotron frequency, $\Omega_e \equiv -q_e B_0 / m_e c$. The electric field component along the velocity is

$$E_{||,v} = \frac{\mathbf{v} \cdot \mathbf{E}}{v_{\perp}} = -\delta E e^{\gamma t} \cos(\theta t - \phi) \quad (11)$$

where $\theta = kv_{||} - \omega_r - \Omega_e$. From the equation of motion, the electron acceleration is

$$\frac{dv_{\perp}}{dt} = -\frac{q_e}{m_e} E_{||,v} = \frac{q_e}{m_e} \delta E e^{\gamma t} \cos(\theta t - \phi) \quad (12)$$

The solution of this equation is

$$v_{\perp} = \frac{q_e \gamma \delta E}{m_e (\gamma^2 + \theta^2)} \left[e^{\gamma t} \left(\cos(\theta t - \phi) + \frac{\theta}{\gamma} \sin(\theta t - \phi) \right) - \left(\cos(\phi) - \frac{\theta}{\gamma} \sin(\phi) \right) \right] + v_{\perp,0} \quad (13)$$

We assume $v_{\perp,0} \approx 0$ to consider scattering from relatively low initial energies, then

$$v_{\perp} \propto \frac{\gamma \delta E}{\gamma^2 + \theta^2} \quad (14)$$

Therefore, the change of the electron kinetic energy in time is

$$\frac{d}{dt} \frac{m_e v_{\perp}^2}{2} = -q_e \mathbf{v}_{\perp} \cdot \mathbf{E} \propto \frac{-\gamma}{\gamma^2 + \theta^2} |\delta E|^2 = \frac{-\gamma}{\gamma^2 + \theta^2} \left(\frac{\omega_r}{kc} \right)^2 |\delta B|^2 \quad (15)$$

where $|\delta E| = (\omega/kc) |\delta B|$. We define the electron scattering factor as

$$\sigma_e \equiv \frac{-\gamma}{\gamma^2 + (kv_{||} - \omega_r - \Omega_e)^2} \left(\frac{\omega_r}{kc} \right)^2 |\delta B|^2. \quad (16)$$

This factor indicates the effectivity of the interaction of electrons and a whistler fluctuation through the cyclotron resonance, and shows that the strength of the resonance becomes broader in velocity but smaller as the damping rate increases.

Acknowledgments. This work was performed under the auspices of the U.S. Department of Energy (DOE). It was supported by the Institute of Geophysics and Planetary Physics at Los Alamos, by the DREAM project and by the Magnetic Turbulence and Kinetic Dissipation project of the Laboratory Directed Research and Development Program at Los Alamos, by Department of Energy Project No. LA06-GPRB-NEM01, and by the Sun-Earth Connection Theory Program and the Solar & Heliospheric Physics SR&T Program of the National Aeronautics and Space Administration.

References

- Crooker, N. U., D. E. Larson, S. W. Kahler, S. M. Lamassa, and H. E. Spence (2003) Suprathermal electron isotropy in high-beta solar wind and its role in heat flux dropouts, *Geophys. Res. Lett.*, *30*, 1619, doi:10.1029/2003GL017036.
- de Koning, C. A., J. T. Gosling, R. M. Skoug, J. T. Steinberg (2006) Widths of suprathermal pitch angle distributions during solar electron bursts: ACE observations, *J. Geophys. Res.*, *111*, A04101, doi:10.1029/2005JA011326.
- de Koning, C. A., J. T. Gosling, R. M. Skoug, J. T. Steinberg (2007) Energy dependence of electron pitch-angle distribution widths in solar bursts, *J. Geophys. Res.*, approved.
- Feldman, W. C., J. R. Asbridge, S. J. Bame, J. T. Gosling, and D. S. Lemons (1978) Characteristic electron variations across simple high-speed solar wind streams, *J. Geophys. Res.*, *83*, 5285.

- 360 Gary, S. P. (1993) *Theory of Space Plasma Microinstabilities*, Cambridge University Press,
361 New York.
- 362 Gary, S. P., W. C. Feldman, D. W. Forslund, and M. D. Montgomery (1975a) Electron
363 heat flux instabilities in the solar wind, *Geophys. Res. Lett.*, *2*, 79.
- 364 Gary, S. P., W. C. Feldman, D. W. Forslund, and M. D. Montgomery (1975b) Heat flux
365 instabilities in the solar wind, *J. Geophys. Res.*, *80*, 4197.
- 366 Gary, S. P., R. M. Skoug, and W. Daughton (1999) Electron heat flux constraints in the
367 solar wind, *Phys. Plasmas*, *6*, 2607.
- 368 Hammond, C. M., W. C. Feldman, D. J. McComas, J. L. Phillips, and R. J. Forsyth (1996),
369 Variation of electron-strahl width in the high-speed solar wind: Ulysses observations,
370 *Astron. Astrophys.*, *316*, 350.
- 371 Lemons, D. S. and W. C. Feldman (1983) Collisional modification to the exospheric theory
372 of solar wind halo electron pitch angle distributions, *J. Geophys. Res.*, *88*, 6881.
- 373 Li, H., S. P. Gary, and O. Stawicki (2001) On the dissipation of magnetic fluctuations in
374 the solar wind, *Geophys. Res. Lett.*, *28*, 1347
- 375 Lin, R. P. (1998) Wind observations of suprathermal electrons in the interplanetary
376 medium, *Space Sci. Rev.*, *86*, 61.
- 377 Ogilvie, K. W., R. Fitzenreiter, and M. Desch (2000) Electrons in the low-density solar
378 wind, *J. Geophys. Res.*, *105*, 27277.
- 379 Pagel, C., N. U. Crooker, D. E. Larson, S. W. Kahler, and M. J. Owens (2005) Under-
380 standing electron heat flux signatures in the solar wind, *J. Geophys. Res.*, *110*, A01103,
381 doi:10.1029/2004JA010767.

- 382 Pagel, C., S. P. Gary, C. A. deKoning, R. M. Skoug, and J. T. Steinberg (2007) Whistler
383 scattering of suprathermal electrons in the solar wind, *J. Geophys. Res.*, in press.
- 384 Pilipp, W. G., H. Miggenrieder, M. D. Montgomery, K. -H. Mülh user, H. Rosenbauer,
385 and R. Schwenn (1987a) Characteristics of electron velocity distribution functions in
386 the solar wind derived from the helios plasma experiment, *J. Geophys. Res.*, *92*, 1075.
- 387 Pilipp, W. G., H. Miggenrieder, K. -H. M  lh  user, H. Rosenbauer, R. Schwenn, and F.
388 M. Neubauer (1987b) Variations of electron distribution functions in the solar wind, *J.*
389 *Geophys. Res.*, *92*, 1103.
- 390 Saito, S. and S. P. Gary (2006) All whistlers are not created equality: scattering of strahl
391 electrons in the solar wind via particle-in-cell simulations, *Geophys. Res. Lett.*, in press.
- 392 Scime, E. E., J. E. Littleton, S. P. Gary, R. Skoug, and N. Lin (2001) Solar cycle variations
393 in the electron heat flux: Ulysses observations, *Geophys. Res. Lett.*, *28*, 2169.
- 394 Smith, C. W., K. Hamilton, B. J. Vasquez, and R. J. Leamon (2006a) Dependence of
395 the dissipation range spectrum of interplanetary magnetic fluctuations on the rate of
396 energy cascade, *Astrophys. J.*, *645*, L85.
- 397 Smith, C. W., B. J. Vasquez, K. Hamilton (2006b) Interplanetary magnetic
398 fluctuation anisotropy in the inertial range, *J. Geophys. Res.*, *111*, A09111,
399 doi:10.1029/2006JA011651.
- 400 Vocks, C. and G. Mann (2003) Generation of suprathermal electrons by resonant wave-
401 particle interaction in the solar corona and wind, *Astrophys. J.*, *593*, 1134.
- 402 Vocks, C., C. Salem, R. P. Lin, and G. Mann (2005) Electron halo and strahl formation
403 in the solar wind by resonant interaction with whistler waves, *Astrophys. J.*, *627*, 540.

Table 1. Initial Fluctuation Parameters for Single Mode Runs.

Run	kc/ω_e	$\omega/ \Omega_e $	ζ_c^+	ζ_h^+	ζ_s^+
A	0.1534	$0.02029 - i0.00000$	-9.115	-2.856	-4.398
B	0.3068	$0.05817 - i0.01162$	-4.425	-1.373	-1.690
C	0.4602	$0.1532 - i0.08474$	-2.686	-0.823	-0.686

Figure 1. A schematic picture showing the relationship between whistler waves and strahl electrons. The solid contour lines indicate the electron velocity distribution. The horizontal and vertical axis are velocities parallel and perpendicular to the background magnetic field. The positive and the negative direction parallel and antiparallel to the magnetic field direct sunward and antisunward. The dashed circle surrounds the strahl component. The dotted and dashed lines indicate the resonant velocity of the electrons with whistler waves at wavenumbers k_0 and k_1 , and the phase speeds $v_{ph,0}$ and $v_{ph,1}$.

Figure 2. Linear theory results of whistler waves; dispersion and ζ_j^+ as functions of the wavenumber. Here $(n_c, n_h, n_s)/n_e = (0.9, 0.1, 0.0)$ (left column) and $(n_c, n_h, n_s)/n_e = (0.85, 0.1, 0.05)$ (right column). Other parameters are as stated in section 3 of the text.

Figure 3. Simulation results for the initial single mode cases described in section 4.1. Electron velocity distributions ($v_{||}$ versus v_y) of electrons at $t|\Omega_e| = 0.0$ (left column) and $t|\Omega_e| = 100.0$ (right column), for Run A (top), Run B (middle), and Run C (bottom).

Figure 4. Simulation results for the initial single mode cases described in section 4.1. The normalized electron scattering factor is plotted as a function of parallel velocity normalized by the core electron thermal velocity. The dotted, solid, and bold lines are for the imposed waves in Runs A, B, and C, respectively. These values are normalized by the largest value in this plot.

Figure 5. Simulation results for the initial broadband spectrum cases described in section 4.2.1. Electron velocity distributions at $t|\Omega_e| = 0$ (left column) and 100.0 (right column), for the runs with initial $|\delta B|^2/B_0^2 = 0.005$ (top) and 0.01 (bottom).

Figure 6. Simulation results for the initial broadband spectrum cases described in section 4.2.1. Wave spectra at $t|\Omega_e| = 0$ (solid lines) and $t|\Omega_e| = 100$ for four cases. The four different symbols represent late-time results for initially imposed energy, $|\delta B|^2/B_0^2 = 0.0025$ (open triangles), 0.005 (solid triangles), 0.01 (open circles), and 0.02 (solid circles).

Figure 7. Simulation results for the initial broadband spectrum cases described in section 4.2.1. Pitch angle width as a function of kinetic energy in two cases, initial $|\delta B|^2/B_0^2 = 0.005$ (left), and 0.01 (right). Open and solid circles denote the width at $t|\Omega_e| = 0$ and 100.0, respectively.

Figure 8. Simulation results for the initial broadband spectrum cases described in section 4.2.1. Pitch angle width at $t|\Omega_e| = 100.0$ as a function of whistler wave energy at three energies, $(v_{\parallel}^2 + v_y^2)/v_c^2 = 20$ (open triangles), 30 (open circles), and 40 (solid circles).

Figure 9. The electron scattering factor for three modes selected from the simulations described in section 4.2.1 as a function of the velocity parallel to the background magnetic field. These values are normalized by the largest value in this plot.

Figure 10. Simulation results for the initial broadband spectrum cases described in section 4.2.2. Contour plots of electron velocity distributions at $t|\Omega_e| = 0.0$ (left column) and 100.0 (right column), with $n_s/n_e = 0.03$ (top) and $n_s/n_e = 0.07$ (bottom).

Figure 11. Simulation results for the initial broadband spectrum cases described in section 4.2.2. Pitch angle widths as functions of electron kinetic energy with $n_s/n_e = 0.03$ (left) and $n_s/n_e = 0.07$ (right) at $t|\Omega_e| = 0$ (open circles) and 100.0 (solid circles).

Figure 12. Simulation results for the initial broadband spectrum cases described in section 4.2.2. Pitch angle width as a function of strahl density. Open triangles, open circles, and solid circles represent the width of the distributions at energies, $(v_{\parallel}^2 + v_y^2)/v_c^2 = 20, 30$, and 40 respectively.

Figure 13. The electron scattering factors for each mode as a function of parallel velocity for the simulations described in Section 4.2.2. Symbols are put at the maximum value of the factor for each mode. Open triangles, open circles, and solid circles represent the maximum factors with the strahl density, $n_s/n_e = 0.03, 0.05, 0.07$. These values are normalized by the largest value in this plot.

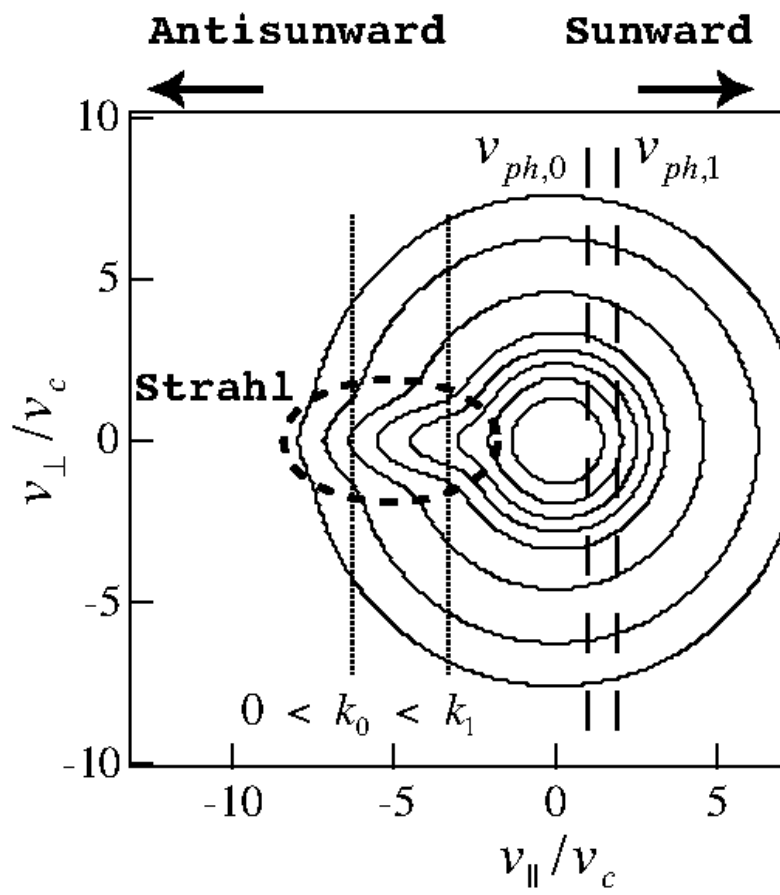


Figure 1

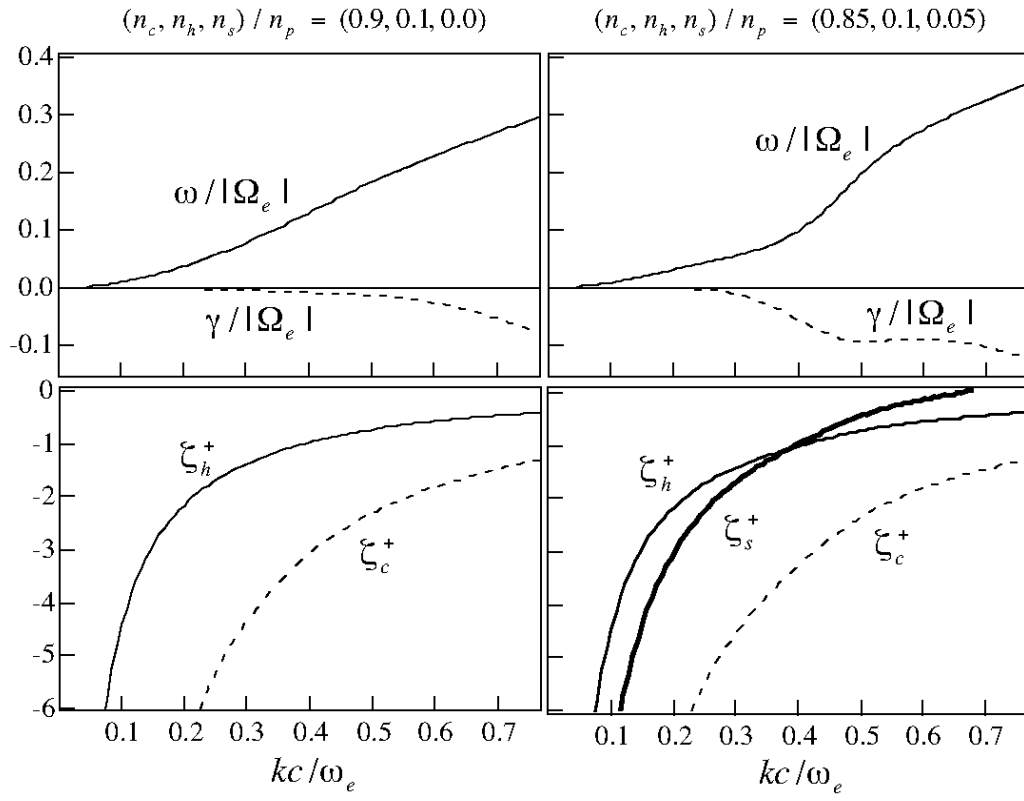


Figure 2

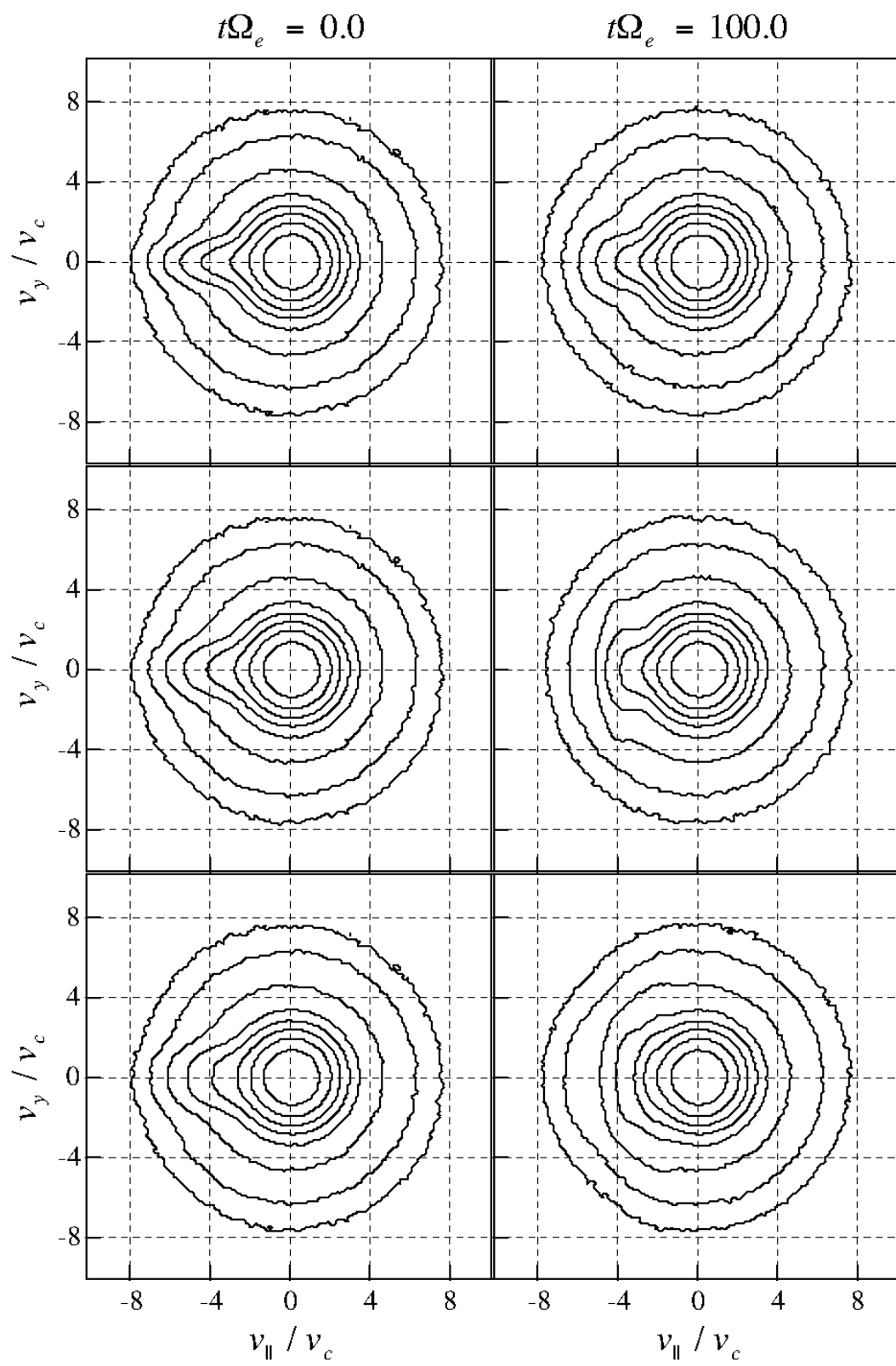


Figure 3

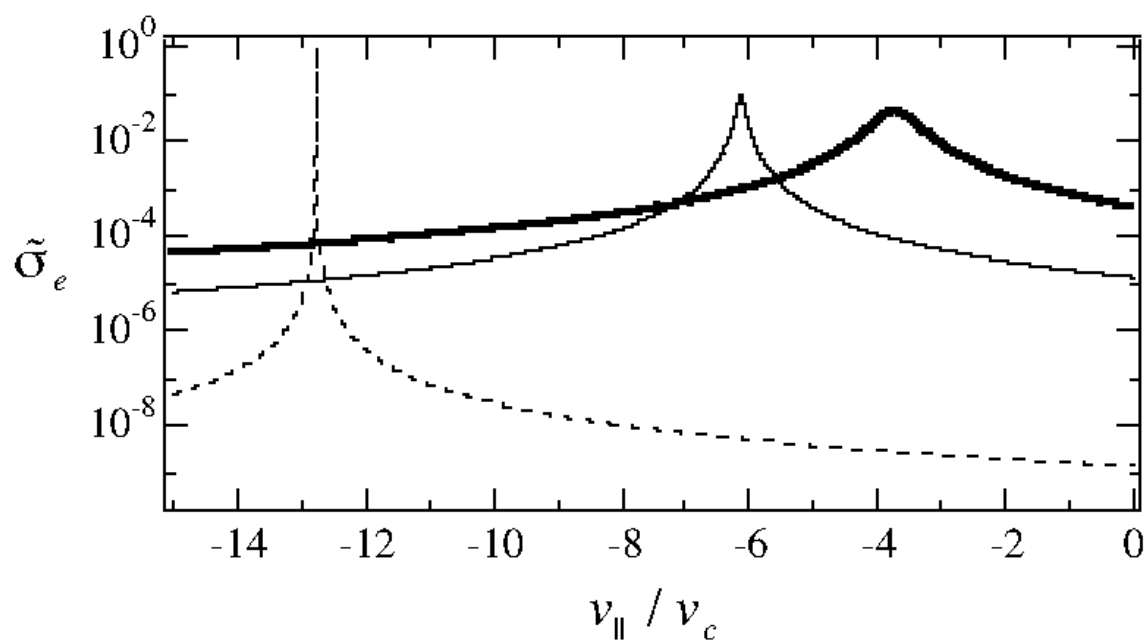


Figure 4

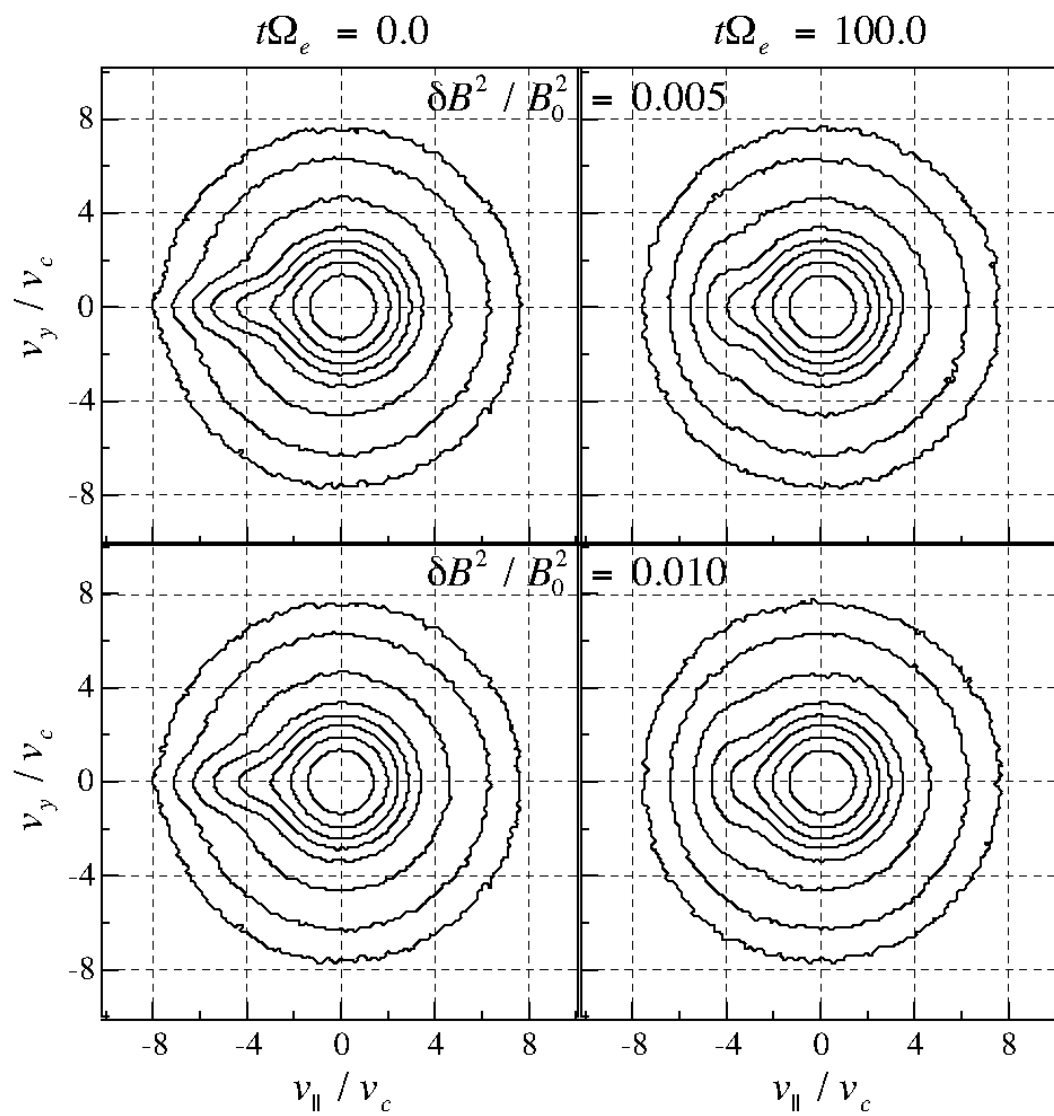


Figure 5

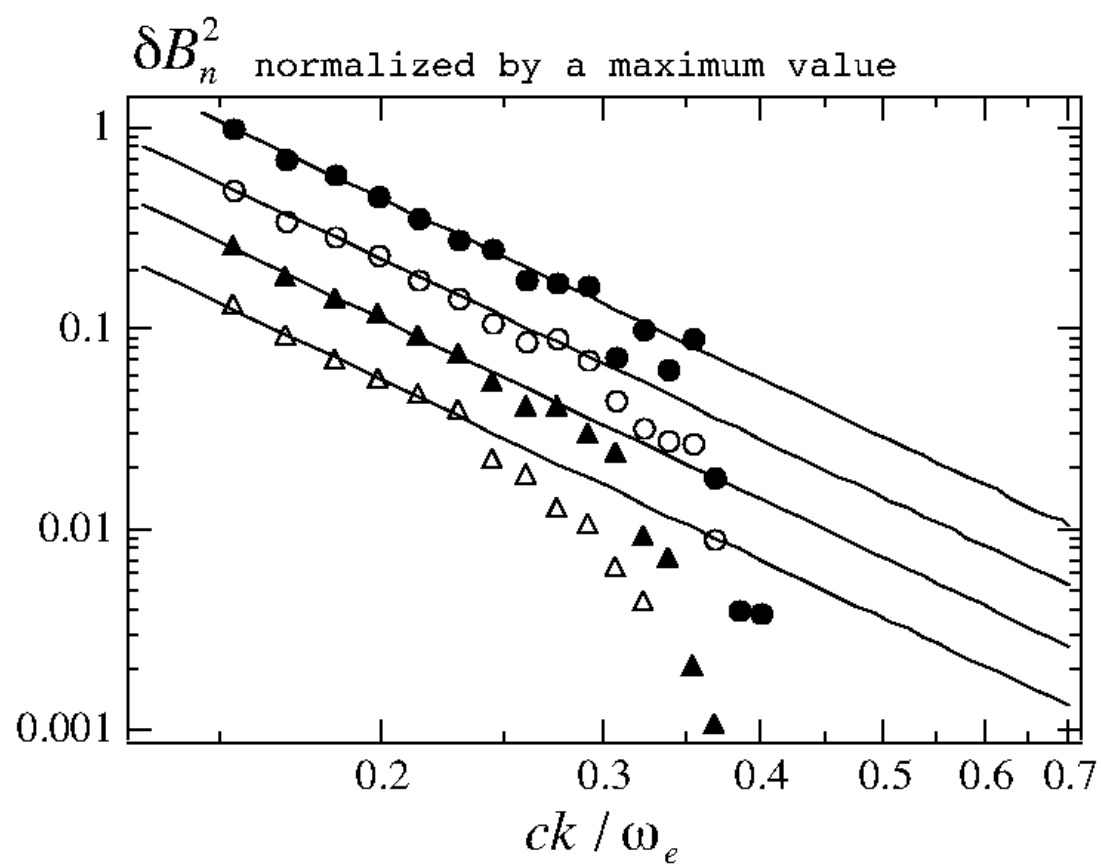


Figure 6

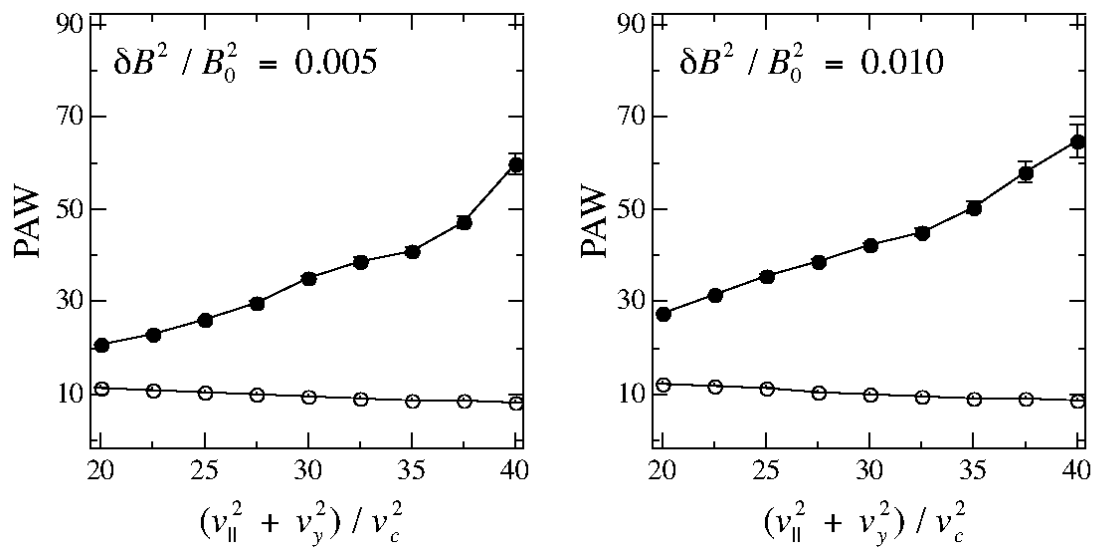


Figure 7

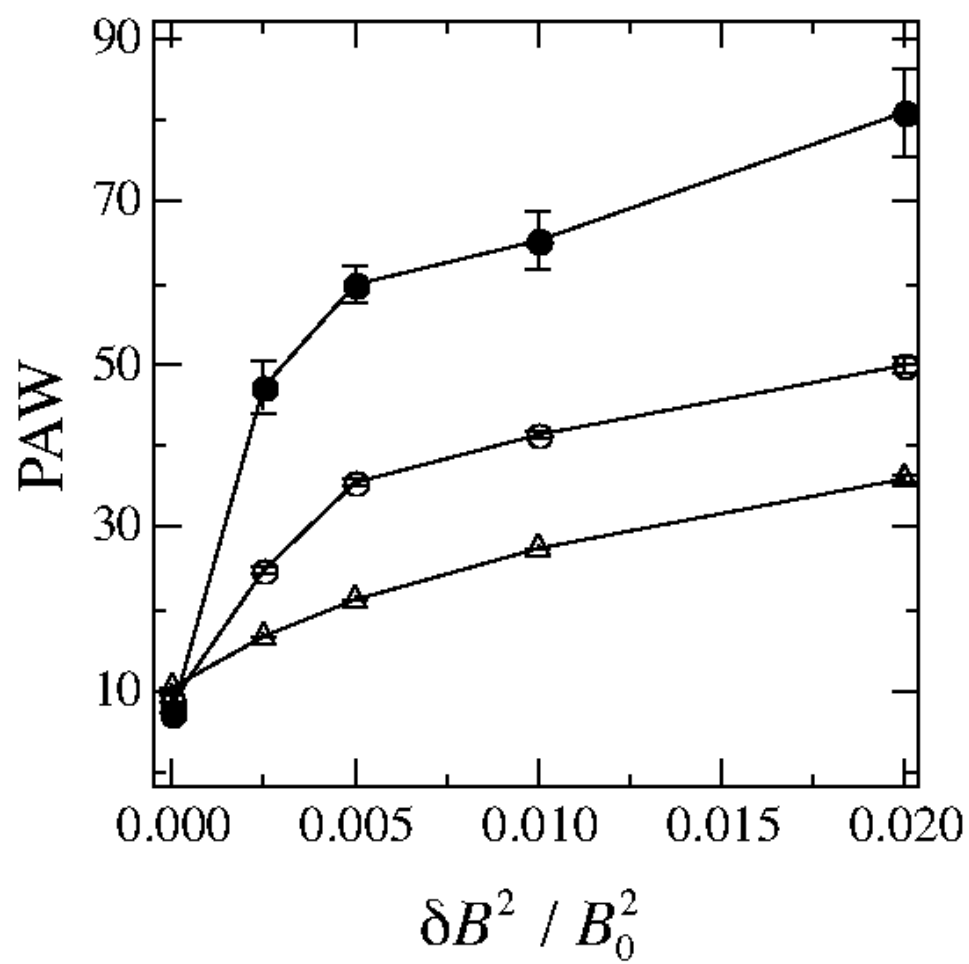


Figure 8

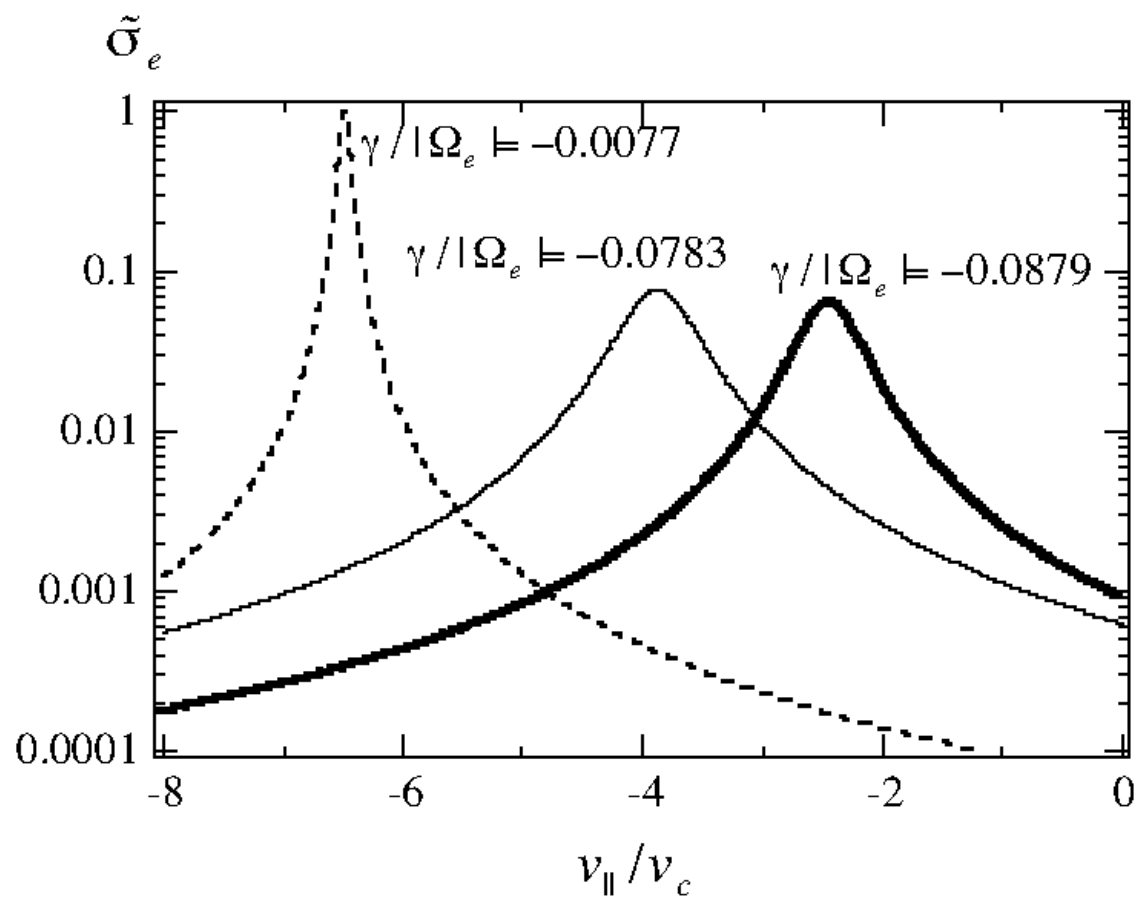


Figure 9

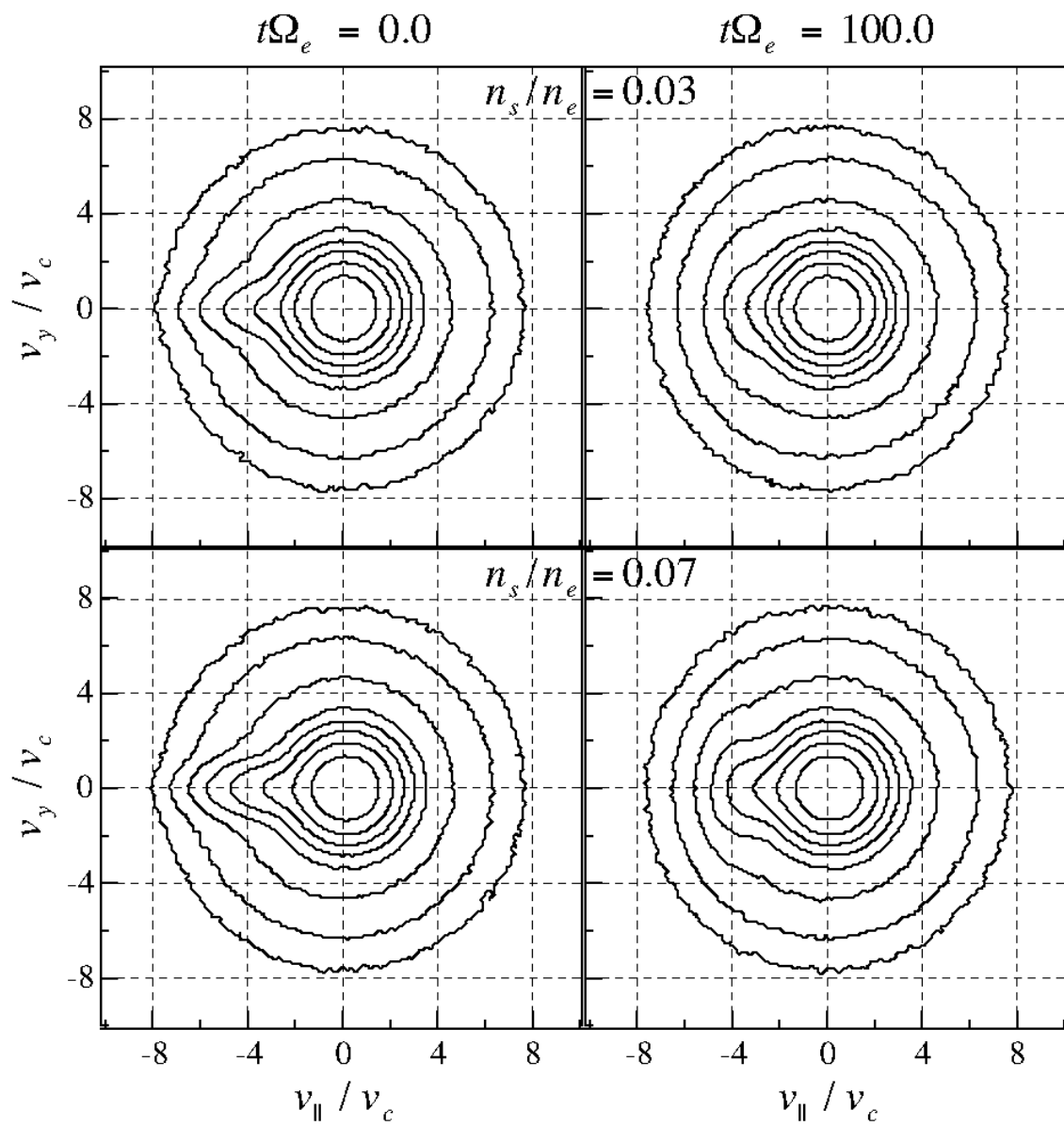


Figure 10

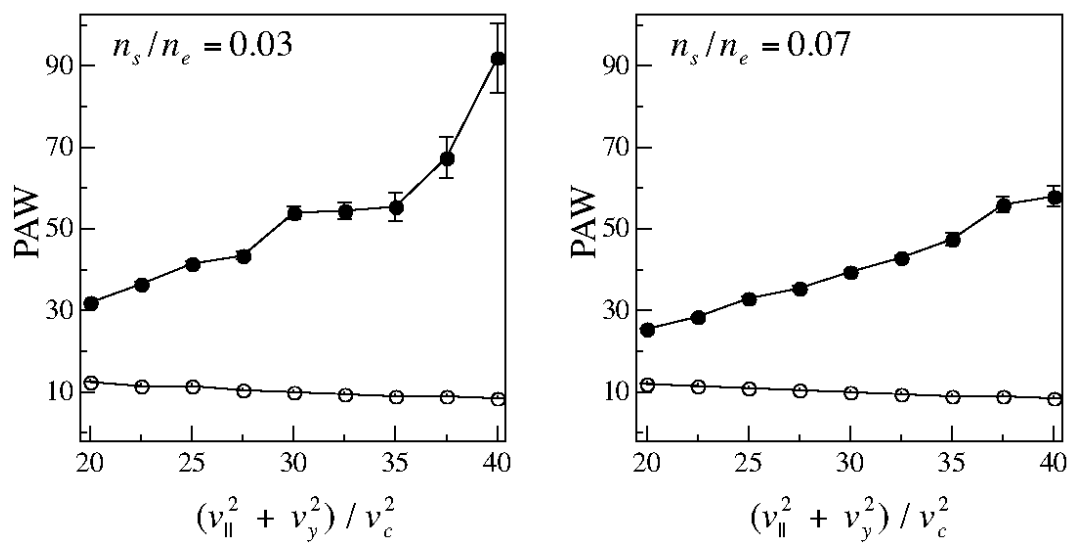


Figure 11

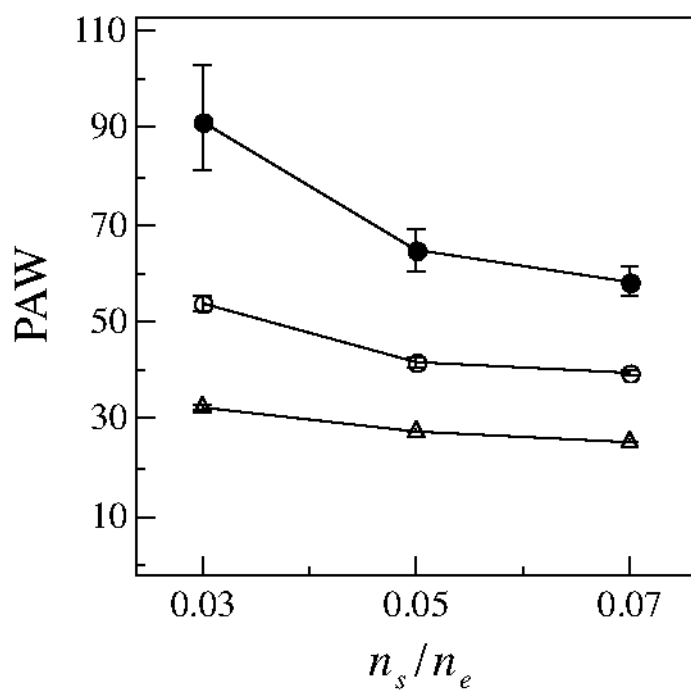


Figure 12

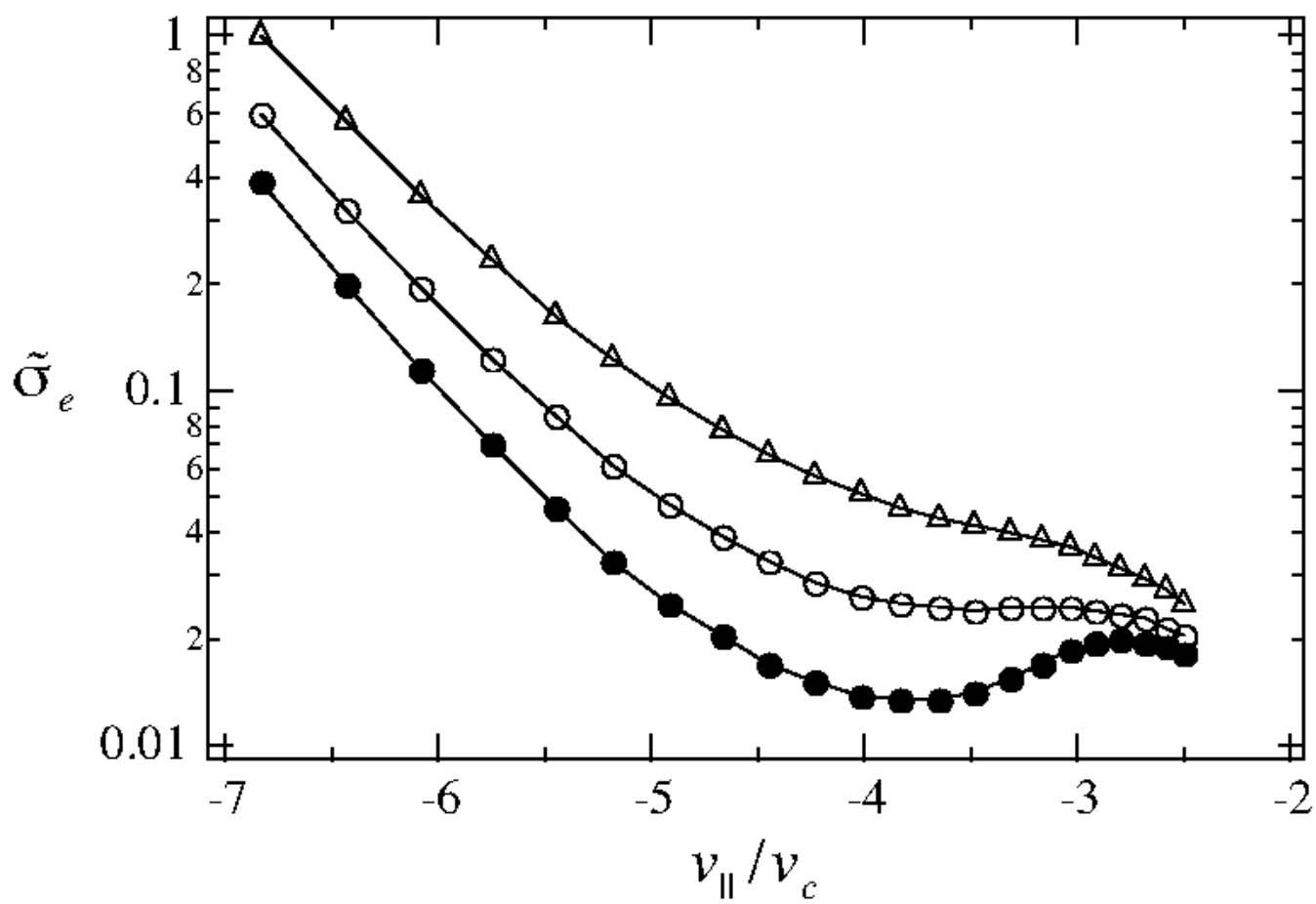


Figure 13